HAL open science

GHOST commissioning science results - II: a very metal-poor star witnessing the early galactic assembly

Federico Sestito, Christian R. Hayes, Kim A. Venn, Jaclyn Jensen, Alan W. Mcconnachie, John Pazder, Fletcher Waller, Anke Ardern-Arentsen, Pascale Jablonka, Nicolas F. Martin, et al.

To cite this version:

Federico Sestito, Christian R. Hayes, Kim A. Venn, Jaclyn Jensen, Alan W. Mcconnachie, et al.. GHOST commissioning science results - II: a very metal-poor star witnessing the early galactic assembly. Monthly Notices of the Royal Astronomical Society, 2024, 528, pp.4838-4851. 10.1093/mnras/stae244 . insu-04465174

HAL Id: insu-04465174

https://insu.hal.science/insu-04465174v1

Submitted on 21 Apr 2024

HAL is a multi-disciplinary open access archive for the deposit and dissemination of scientific research documents, whether they are published or not. The documents may come from teaching and research institutions in France or abroad, or from public or private research centers.

L'archive ouverte pluridisciplinaire **HAL**, est destinée au dépôt et à la diffusion de documents scientifiques de niveau recherche, publiés ou non, émanant des établissements d'enseignement et de recherche français ou étrangers, des laboratoires publics ou privés.

Distributed under a Creative Commons Attribution 4.0 International License

Monthly Notices of the ROYAL ASTRONOMICAL SOCIETY

MNRAS **528,** 4838–4851 (2024)
Advance Access publication 2024 February 6

https://doi.org/10.1093/mnras/stae244

GHOST commissioning science results – II: a very metal-poor star witnessing the early galactic assembly

Federico Sestito,[1★] Christian R. Hayes,[2] Kim A. Venn,[1] Jaclyn Jensen,[1] Alan W. McConnachie,[1,2] John Pazder,[1,2] Fletcher Waller,[1] Anke Ardern-Arentsen,[3] Pascale Jablonka,[4,5] Nicolas F. Martin,[6,7] Tadafumi Matsuno,[8] Julio F. Navarro,[1] Else Starkenburg,[8] Sara Vitali,[9] John Bassett,[10] Trystyn A. M. Berg,[2,11] Ruben Diaz,[10] Michael L. Edgar,[12] Veronica Firpo,[10] Manuel Gomez-Jimenez,[10] Venu Kalari,[10] Sam Lambert,[2] Jon Lawrence,[13] Gordon Robertson,[13] Roque Ruiz-Carmona,[10] Ricardo Salinas,[10] Kim M. Sebo[14] and Sudharshan Venkatesan[13]

Affiliations are listed at the end of the paper

Accepted 2024 January 19. Received 2024 January 4; in original form 2023 August 13

ABSTRACT

This study focuses on Pristine_180956.78−294759.8 (hereafter P180956, [Fe/H] = −1.95 ± 0.02), a star selected from the Pristine Inner Galaxy Survey (PIGS), and followed-up with the recently commissioned Gemini High-resolution Optical SpecTrograph (GHOST) at the Gemini South telescope. The GHOST spectrograph's high efficiency in the blue spectral region (3700−4800 Å) enables the detection of elemental tracers of early supernovae (e.g. Al, Mn, Sr, and Eu). The star exhibits chemical signatures resembling those found in ultrafaint dwarf (UFD) systems, characterized by very low abundances of neutron-capture elements (Sr, Ba, and Eu), which are uncommon among stars in the Milky Way halo. Our analysis suggests that P180956 bears the chemical imprints of a small number (2 or 4) of low-mass hypernovae ($\sim 10-15\,M_\odot$), which are needed to mostly reproduce the abundance pattern of the light-elements (e.g. [Si, Ti/Mg, Ca] ∼0.6), and one fast-rotating intermediate-mass supernova ($\sim 300\,\mathrm{km\,s^{-1}}$, $\sim 80-120\,M_\odot$), which is the main channel contributing to the high [Sr/Ba] (∼+1.2). The small pericentric (∼ 0.7 kpc) and apocentric (∼ 13 kpc) distances and its orbit confined to the plane ($\lesssim 2$ kpc) indicate that this star was likely accreted during the early Galactic assembly phase. Its chemo-dynamical properties suggest that P180956 formed in a system similar to a UFD galaxy accreted either alone, as one of the low-mass building blocks of the proto-Galaxy, or as a satellite of Gaia–Sausage–Enceladus. The combination of Gemini's large aperture with GHOST's high efficiency and broad spectral coverage makes this new spectrograph one of the leading instruments for near-field cosmology investigations.

Key words: stars: kinematics and dynamics – stars: Population II – Galaxy: abundances – Galaxy: bulge – Galaxy: evolution – Galaxy: formation.

1 INTRODUCTION

Low-metallicity stars are among the oldest stars in the Galaxy. Cosmological simulations suggest that most metal-poor stars formed within 2−3 Gyr after the big bang, likely in low-mass systems that were accreted early on into the Galaxy ('building blocks', e.g. Starkenburg et al. 2017a; El-Badry et al. 2018; Sestito et al. 2021). These merging building blocks contributed stars, gas, and dark matter to the proto-Milky Way (proto-MW). Because they formed at the bottom of the potential well of the merging building blocks, these stars are predicted to occupy the inner regions of the present-day Galaxy (e.g. White & Springel 2000; Starkenburg et al. 2017a; El-Badry et al. 2018; Sestito et al. 2021). Systems accreted later are anticipated to disperse their stars primarily in the halo (Bullock & Johnston 2005; Johnston et al. 2008; Tissera et al. 2012), or possibly the disc (e.g. Abadi et al. 2003; Santistevan et al. 2021; Sestito et al. 2021). An *in situ* component may also form from the gas deposited by the building blocks, recently called the Aurora stars (Belokurov & Kravtsov 2022). This *in situ* component may have formed in a lumpy and chaotic interstellar medium (ISM), possibly resembling the chemical properties of globular clusters (GCs; Belokurov & Kravtsov 2023).

The most chemically pristine stars in the MW may have been enriched by only one or a few supernovae or hypernovae events (e.g. Frebel et al. 2010a; Ishigaki et al. 2018). The study of the orbital properties and chemical abundance patterns of pristine stars is essential for understanding the lives and deaths of the first stars and the assembly history of the Galaxy (e.g. Freeman & Bland-Hawthorn 2002; Venn et al. 2004; Tumlinson 2010; Wise et al. 2012; Karlsson et al. 2013).

★ E-mail: sestitof@uvic.ca

© 2024 The Author(s).
Published by Oxford University Press on behalf of Royal Astronomical Society. This is an Open Access article distributed under the terms of the Creative Commons Attribution License (http://creativecommons.org/licenses/by/4.0/), which permits unrestricted reuse, distribution, and reproduction in any medium, provided the original work is properly cited.

Downloaded from https://academic.oup.com/mnras/article/528/3/4838/7602409 by guest on 21 April 2024

Metal-poor stars in and towards the Galactic bulge can serve as important tracers of the earliest stages of Galactic assembly, yet their detection is extremely challenging (e.g. Schlaufman & Casey 2014; Lamb et al. 2017). The inner regions of the MW are dominated by a metal-rich population and disrupted GCs (Bensby et al. 2013; Ness et al. 2013a, 2014; Bensby et al. 2017; Schiavon et al. 2017; Schultheis et al. 2019). Furthermore, extreme interstellar extinction and stellar crowding have made photometric surveys of bulge metal-poor stars exceedingly difficult.

The Abundances and Radial velocity Galactic Origins Survey (Ness et al. 2013b) found that $\lesssim 1$ percent of their sample had [Fe/H][1] <-1.5, resulting in a total of 84 stars. The metallicity-sensitive photometric filter from the SkyMapper Southern Survey (Bessell et al. 2011; Wolf et al. 2018) has been used by the Extremely Metal-poor BuLge stars with AAOmega (EMBLA, Howes et al. 2014, 2015, 2016) survey to select very metal-poor stars (VMPs, [Fe/H] ≤ -2.0). Their high-resolution analysis of 63 VMPs revealed that the majority resembled chemically metal-poor stars in the Galactic halo, with the exception of a lack of carbon-rich stars and a larger scatter in [α/Fe] abundances. Additionally, their kinematic analysis found that it was challenging to distinguish stars that were born in the bulge from those that are merely in the inner halo. The Chemical Origins of Metal-poor Bulge Stars (Lucey et al. 2019) studied the chemo-dynamical properties of inner Galactic stars, finding that around $\sim$50 percent of their sample is composed of halo interlopers, while their chemical properties resemble those of the halo (Lucey et al. 2021, 2022).

Similar to the EMBLA survey, the Pristine Inner Galaxy Survey (PIGS, Arentsen et al. 2020a, b) selected metal-poor targets from the narrow-band photometry of the Pristine survey (Starkenburg et al. 2017b). The Pristine survey, conducted at the Canada–France–Hawaii Telescope (CFHT), utilizes the CaHK filter in combination with broad-band photometry to provide a highly efficient method of identifying low-metallicity stars ($\sim$56 per cent success rate at [Fe/H] ≤ -2.5, Youakim et al. 2017; Aguado et al. 2019; Venn et al. 2020; Lucchesi et al. 2022). Around $\sim$12 000 inner Galaxy metal-poor candidates selected by PIGS were observed with low-/medium-resolution spectroscopy using the AAOmega spectrograph on the Anglo Australian Telescope (AAT). The results of these observations showed $\sim$80 per cent efficiency in identifying VMP stars towards the bulge (Arentsen et al. 2020b) and the Sagittarius dwarf galaxy (DG; Vitali et al. 2022) using the Pristine metallicity-sensitive filter for initial selection. Interestingly, within PIGS, Mashonkina et al. (2023) report the serendipitous discovery of the first r- and s-processes rich Carbon-enhanced star (CEMP−r/s) in the inner Galaxy.

In a recent study, Sestito et al. (2023a) analysed high-resolution spectra of 17 metal-poor stars selected from the PIGS survey taken with the Gemini Remote Access to CFHT ESPaDOnS Spectrograph (GRACES, Chene et al. 2014; Pazder et al. 2014). Their findings, consistent with Howes et al. (2016), indicate that the chemo-dynamical properties of the VMP population in the inner Galaxy resemble that of the halo, suggesting a common origin from disrupted building blocks. Sestito et al. (2023a) report stars with chemical abundances compatible with those of disrupted second-generation GCs, one with exceptionally low metallicity ([Fe/H] ~ -3.3), well below the metallicity floor of GCs ([Fe/H] ~ -2.8, Beasley et al. 2019). This provides further evidence that extremely metal-poor structures (EMPs, [Fe/H] ≤ -3.0) can form in the early Universe (see also Martin et al. 2022, on the discovery of the disrupted EMP GC, C-19).

In this paper, we present a new analysis of the inner Galactic VMP Pristine_180956.78−294759.8 (P180956), from spectra taken during the commissioning of the new Gemini High-resolution Optical SpecTrograph (GHOST, Pazder et al. 2020). This star was previously analysed in the PIGS/GRACES analysis (Sestito et al. 2023a), but it can be observed from either the northern hemisphere (GRACES) or the south (GHOST, at Gemini South). P180956 is selected for this work for its unusually low [Na, Ca/Mg] and [Ba/Fe] ratios and for its high eccentric orbit that remains confined close to the MW plane. The new GHOST spectrograph has also been used in the analysis of two stars in the Reticulum II ultrafaint dwarf (UFD) galaxy (Hayes et al. 2023), and the presentation of the spectrum of the r-process rich standard star HD 222925 (Hayes et al. 2022; McConnachie et al. 2022). GHOST's wide spectral coverage and its high efficiency in the blue region are crucial to detect species that are tracers of the early chemical evolution (e.g. Al, Mn, Sr, Eu) and that were not accessible with GRACES spectrograph.

The instrument setup and data reduction are described in Section 2. Sections 3 and 4 discuss the model atmospheres analysis and the chemical abundance analyses, respectively. Orbital parameters are reported in Section 5. The results are discussed in Section 6, focusing on the type of supernovae that polluted the formation site of P180956, and its origin in an ancient dwarf system, which may have resembled today's UFDs. Conclusions are presented in Section 7.

2 DATA

2.1 GHOST observations

The target (G =13.50 mag), P180956, was initially observed as part of the PIGS photometric survey using MegaCam at the CFHT. Its small pericentric distance ($r_{\rm peri} \sim 0.7$ kpc), the apocentre ($\sim$ 13 kpc), the limited maximum excursion from the plane ($Z_{\rm max} \sim 1.8$ kpc), and its high eccentricity ($\epsilon \sim 0.90$) imply that it was likely accreted during the early stages of Galactic assembly (Sestito et al. 2023a). A low/medium-resolution ($R \sim$1300 and 11 000) spectrum of P180956 was obtained using AAT/AAOmega (Arentsen et al. 2020b), and also with the Gemini Remote Access to CFHT ESPaDOnS Spectrograph (GRACES, $R \sim$40000, Chene et al. 2014; Pazder et al. 2014) as part of LLP-102 (PI K.A. Venn). The GRACES spectrum was analysed by Sestito et al. (2023a) along with 16 other VMP stars in the Galactic bulge; however, due to limitations in the throughput of the 300-m optical fiber, the bluest spectral regions were not accessible for that study. The GRACES spectral analysis was limited to a range of 4900−10000 Å only. Thus, P180956 was chosen as a commissioning target for the Gemini High-resolution Optical SpecTrograph (GHOST, Pazder et al. 2020). The instrument's high efficiency in the blue spectral region makes it ideal for detecting spectral features of additional chemical elements which allow a deeper investigation of the origins of P180956.

The target was observed on 2022 September 12, during the second commissioning run of GHOST. Three exposures, each lasting 600 s, were conducted. The instrument was configured in the standard resolution ($R \sim$50 000) single object mode, employing a spectral and spatial binning of 2 and 4, respectively. The instrument setup allows to cover the 3630−5440 Å region with the blue arm and the 5210−9500 Å region with the red arm. This specific setup and exposure times were chosen to enable the detection of spectral lines from species in the bluer regions ($\sim$4000 Å) of the spectrum that were not accessible with GRACES, i.e. C, Al, Si, Sc, V, Mn, Co,

[1] [Fe/H]= $\log(N_{\rm Fe}/N_{\rm H})_\star - \log(N_{\rm Fe}/N_{\rm H})_\odot$, where N_X represents the number density of element X.

Downloaded from https://academic.oup.com/mnras/article/528/3/4838/7602409 by guest on 21 April 2024

Table 1. Log of the observations.

Property	Value
Pristine name	Pristine_180956.78−294759.8
Source ID	4050071013878221696
RA	272.4865677802622
Dec	−29.799952273156627
G	13.50 mag
BP − RP	1.55 mag
$E(B-V)$	0.53 mag
$t_{\rm exp}$	1800 s
$N_{\rm exp}$	3
SNR @Eu II, @Mg Ib, @Na I	16, 50, 65
RV	262.976 ± 0.363 km s^{-1}
$T_{\rm eff}$	5391 ± 133 K
log g	1.87 ± 0.10

Notes. The Pristine name, the short name, the source ID, G, and BP − RP from *Gaia* DR3, the reddening from the 3D map of Green et al. (2019), the total exposure time, the number of exposures, the SNR, and the radial velocity are reported. The SNR is measured as the ratio between the median flux and its standard deviation in three spectral regions, close to the Eu II 4129 Å, in the Mg Ib Triplet and in the Na I Doublet.

Cu, Zn, Sr, Y, La, Eu. Table 1 reports the *Gaia* DR3 source ID and photometry, the reddening from Green et al. (2019) along with the total exposure time and the number of exposures.

2.2 Data reduction

The acquired spectra were processed using the GHOST Data Reduction pipeline (Ireland et al. 2018; Hayes et al. 2022), which is integrated into the DRAGONS suite (Labrie et al. 2019). This pipeline[2] generates 1D spectra for the blue and red arms, which were wavelength calibrated, order combined, and sky subtracted. Subsequently, the spectra were individually normalized through polynomial fitting, and barycentric corrections were applied. Radial velocities and their uncertainties have been measured for the blue and red arms using the DOPPLER code,[3] which cross-correlate the observed spectra with a VMP template synthesized with TURBOSPECTRUM[4] (Plez 2012) and a MARCS[5] model atmosphere (Gustafsson et al. 2008). The radial velocity measured from the blue and red arms are RV $= 263.034 \pm 0.020$ km s^{-1} and RV $= 262.918 \pm 0.362$ km s^{-1}, respectively. Their average, RV $= 262.976 \pm 0.363$ km s^{-1}, is in agreement within 0.8σ from the measurement in the GRACES analysis (RV $= 262.45 \pm 0.54$ km s^{-1}, Sestito et al. 2023a) and by 2.3σ with the value from the low-/medium-resolution PIGS campaign (RV $= 264.86 \pm 0.73$ km s^{-1}, Arentsen et al. 2020a). The lack of RV variation likely rules out the possibility that the object is in a binary system. The continuum points in the observations were identified using spectral templates and fitted via an iterative sigma clipping method to obtain a normalized spectrum. Finally, the blue and red output spectra were merged together with inverse-variance weighting in the overlapping regions.

Fig. 1 showcases the reduced spectrum of P180956. In the top panel, a comparison is made with the GRACES observation in the 4400−5200 Å region. Both instruments have similar spectral (high) resolution; however, the signal-to noise ratio (SNR) of the GRACES spectrum (black line) deteriorates below 5000 Å, a region where the number of spectral lines clearly increases, as seen in the GHOST spectrum (blue). The Balmer line H−ϵ, the Ca II H&K lines, along with two Al I lines, two Ti I, five Fe I lines, and one Co I line are shown in the central panel. The Mg Ib Triplet (∼5180 Å) region also contains several Fe and Ti lines, as shown in the bottom panel. Table 1 reports the SNR measured close to the Eu II 4129 Å line, the Mg Ib Triplet region, and to the Na I Doublet (∼5890 Å).

3 MODEL ATMOSPHERES ANALYSIS

3.1 Stellar parameters

The stellar parameters used in this study are adopted from the GRACES analysis by Sestito et al. (2023a, $T_{\rm eff} = 5391 \pm 133$ K, log g $=1.87 \pm 0.10$). To briefly summarize, the effective temperature is estimated based on the colour–temperature relationship derived by Mucciarelli et al. (2021). This relationship is based on the Infrared Flux Method introduced by González Hernández & Bonifacio (2009) and adapted to the *Gaia* EDR3 photometry. The surface gravity is determined by applying the Stefan-Boltzmann equation, inferred assuming a flat mass distribution between 0.5 and 0.8 M$_\odot$. These calculations rely on several factors: (1) the de-reddened photometry[6]; (2) the distance to the star, which is estimated to be 3.30 ± 0.27 kpc (Sestito et al. 2023a); and (3) a metallicity (taken as [Fe/H] $= -2.0 \pm 0.1$, Sestito et al. 2023a). Uncertainties on the stellar parameters are derived using a Monte Carlo simulation.

The microturbulence velocity ($v_{\rm micro}$) is obtained spectroscopically achieving a flatter distribution in the abundances from the Fe I lines, A(Fe I)[7] versus the reduced equivalent width. This gives a $v_{\rm micro} = 1.5 \pm 0.1$ km s^{-1}.

3.2 Spectral lines and atomic data

The spectral line list is generated with LINEMAKE (Placco et al. 2021), including lines with hyper-fine structure corrections (Sc, V, Mn, Co, and Cu), molecular bands (CH in the 4300 Å region) and r-process isotopic corrections (Ba and Eu). For CH, a ratio of ^{12}C/^{13}C =5 has been assumed as for a typical RGB star (Spite et al. 2006). Solar abundances are taken from Asplund et al. (2009).

An initial measurement of the equivalent width is performed using DAOSPEC (Stetson & Pancino 2008), which automatically fits Gaussian profiles to spectra following the input line list. Given the SNR of our spectrum, lines weaker than 15 mÅ are rejected, and lines stronger than 100 mÅ are further examined with non-Gaussian measurements, i.e. with an integral. The equivalent widths are then used with the MOOG[8] spectrum synthesis code (Sneden 1973; Sobeck et al. 2011) to determine the chemical abundances assuming local thermodynamic equilibrium (LTE). The spherical MARCS[9] model atmospheres (Gustafsson et al. 2008; Plez 2012), which assume [α/Fe] =0.4, are used for the chemical abundance analysis in this paper, which yield to [Fe/H] $= -1.95 \pm 0.02$. The

[2]https://github.com/GeminiDRSoftware/GHOSTDR
[3]https://github.com/dnidever/doppler
[4]https://github.com/bertrandplez/Turbospectrum2019
[5]https://marcs.astro.uu.se

[6]Extinction is from the 3D map of Green et al. (2019). To convert from the $E(B-V)$ map to *Gaia* extinction coefficients, the $A_V/E(B-V) = 3.1$ (Schultz & Wiemer 1975) and the $A_G/A_V = 0.85926$, $A_{BP}/A_V = 1.06794$, $A_{RP}/A_V = 0.65199$ relations (Marigo et al. 2008; Evans et al. 2018) are used.
[7]$A(X) = 12 + \mathrm{Log}(N_X/N_H)$
[8]https://www.as.utexas.edu/~chris/moog.html
[9]https://marcs.astro.uu.se

Downloaded from https://academic.oup.com/mnras/article/528/3/4838/7602409 by guest on 21 April 2024

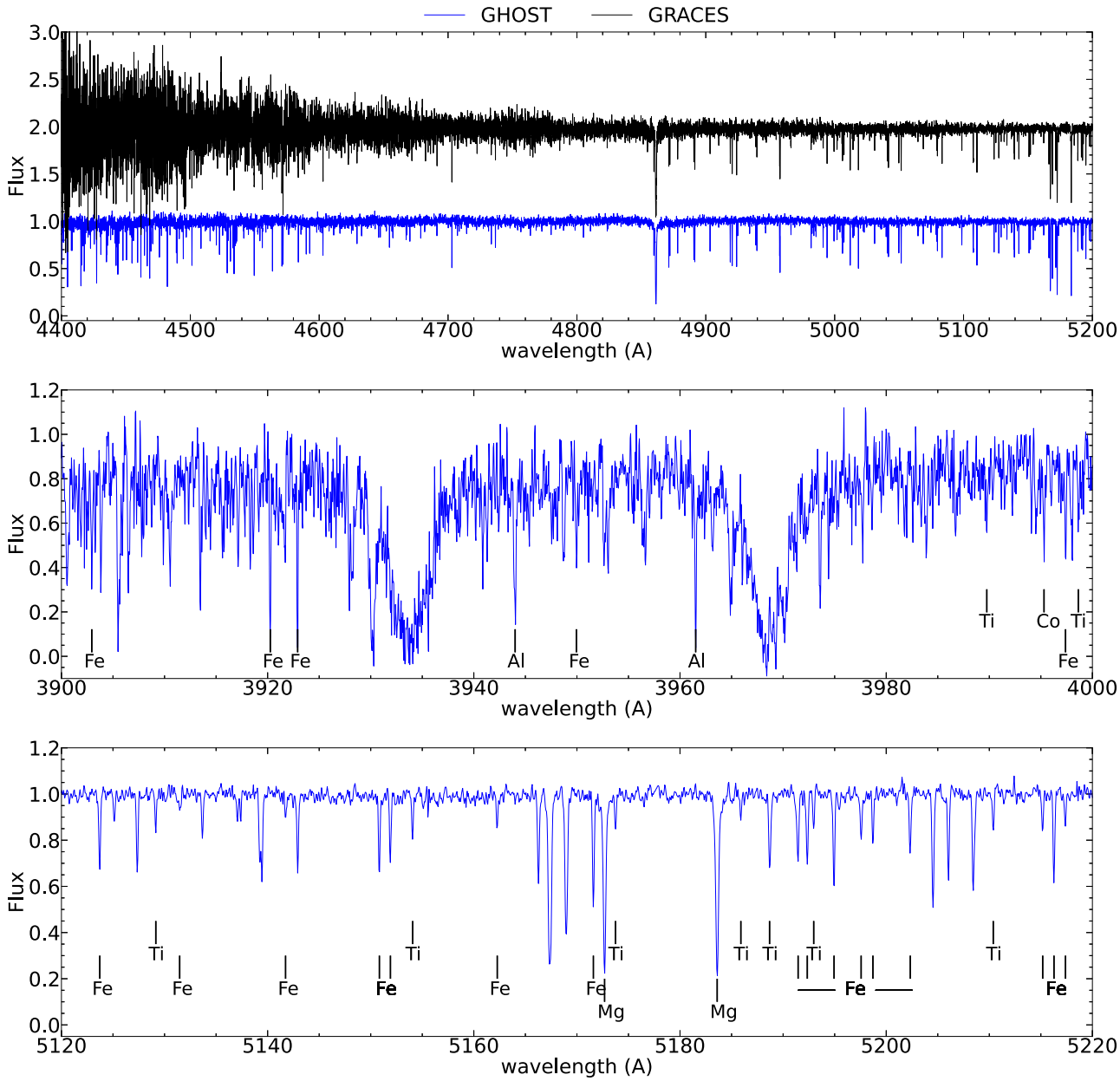

Figure 1. GHOST spectrum of P180956. Top panel: wide spectral region, 4400−5200 Å, also showing the GRACES spectrum (black line). Central panel: blue region 3900−4000 Å. Bottom panel: Mg Ib Triplet. Spectral lines used for the chemical abundance analysis are marked.

chemical abundances of Sc, Cu, Y, Ba, La, and Eu are determined using the SYNTH mode within MOOG.

The list of spectral lines used for the chemical abundance analysis, their atomic data, their EWs and abundances are reported as supplementary online material.

3.3 Uncertainties on the chemical abundances

MOOG provides estimates of the chemical abundances A(X) along with their line-to-line scatter, $\delta_{A(X)}$. The total abundance scatters, $\delta_{A(X),\,TOT}$, are calculated by combining in quadrature the line-to-line scatter with the uncertainties resulting from variations in the stellar parameters ($\delta_{T_{eff}}$, $\delta_{\log g}$, both ∼0.02), in the microturbulence velocity ($\delta_{v_{micro}} \sim 0.02$) and in the metallicity ($\delta_{[Fe/H]} \sim 0.02$). The final uncertainty for element X is given by $\sigma_{A(X)} = \delta_{A(X),TOT}/\sqrt{N_X}$. In case, there is only one spectral line or SYNTH mode is employed, the dispersion in Fe I lines is considered as the typical dispersion.

4 CHEMICAL ABUNDANCE ANALYSIS

The blue wavelength coverage of GHOST permits an analysis of the spectral lines of many elements in metal-poor stars, including a range of α-, odd-Z, Fe-peak, and neutron-capture process elements.

4.1 Carbon

Carbon was first inferred from the low-/medium-resolution campaign of PIGS (Arentsen et al. 2020a), showing the star is Carbon-normal, [C/Fe] =0.17 ± 0.24. Fig. 2 shows the synthesis on the CH bands (Masseron et al. 2014) in the 4300 Å region (top panel) and the

Downloaded from https://academic.oup.com/mnras/article/528/3/4838/7602409 by guest on 21 April 2024

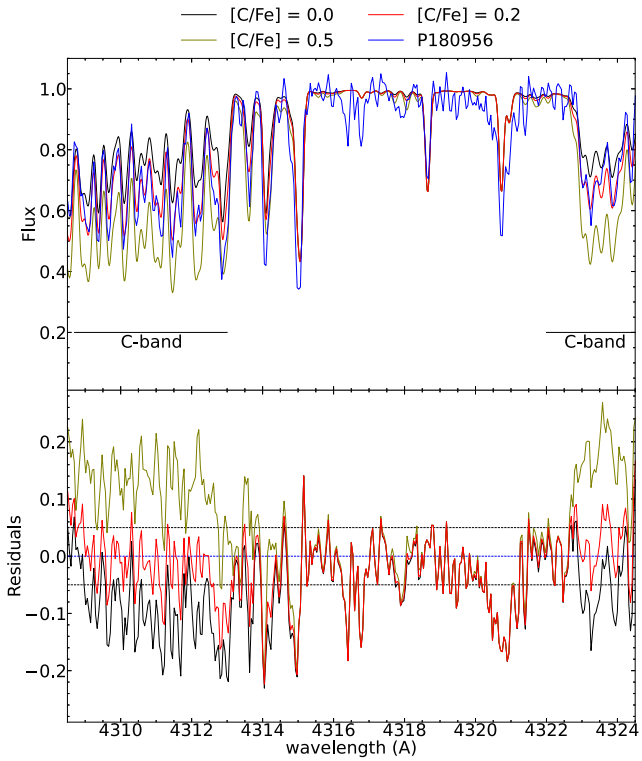

Figure 2. Carbon synthesis. Top panel: the observed spectrum of P180956 is marked with a blue line, while synthetic spectra are denoted by black ([C/Fe] =0.0), red ([C/Fe] =0.2, best fit), and olive ([C/Fe] =0.5) lines. Bottom panel: residuals of the fits. Horizontal dashed lines mark the null difference (blue) and the dispersion around the continuum (±0.05 dex, black). The residuals of the best fit (red line) in the regions of Carbon bands are within or similar to the level of the continuum dispersion.

residuals (bottom panel). The synthesis is made with SYNTH mode of MOOG, yielding a [C/Fe] $=0.2 \pm 0.1$, in agreement with the previous measurement. The evolutionary correction for [C/Fe] is inferred using the relation from Placco et al. (2014), which is 0.13 dex, providing a final [C/Fe] $=0.33 \pm 0.10$.

4.2 α-elements

The α-elements producing detectable lines in this star are Mg, Si, Ca, and Ti (Lawler et al. 2013; Wood et al. 2013; Den Hartog et al. 2021; Kramida et al. 2021; Den Hartog et al. 2023). The A(Mg I) is from two lines of the Mg I Triplet (λλ5172.684, 5183.604 Å) and from other five lines for which the SNR is high (>15). Si I is detected from the 4102.936 Å line, which is blended with the wing of the broader Hδ line. The A(Ca I) is inferred from 17 spectral lines, from 4200 to 6500 Å. The Ca Triplet has been excluded since it shows strong lines (>140 mÅ). Ti I and Ti II are present with 17 and 30 lines, respectively.

4.3 Odd-Z elements

Four odd-Z elements are detectable in the GHOST spectrum of this object, Na, Al, K, and Sc (Lawler et al. 2019; Kramida et al. 2021; Roederer & Lawler 2021). Na I is present with the Na I Doublet (λλ5889.951, 5895.924 Å). The Na I D lines from the interstellar medium are not affecting the stellar component, in agreement with Sestito et al. (2023a). The combination of the wide spectral coverage

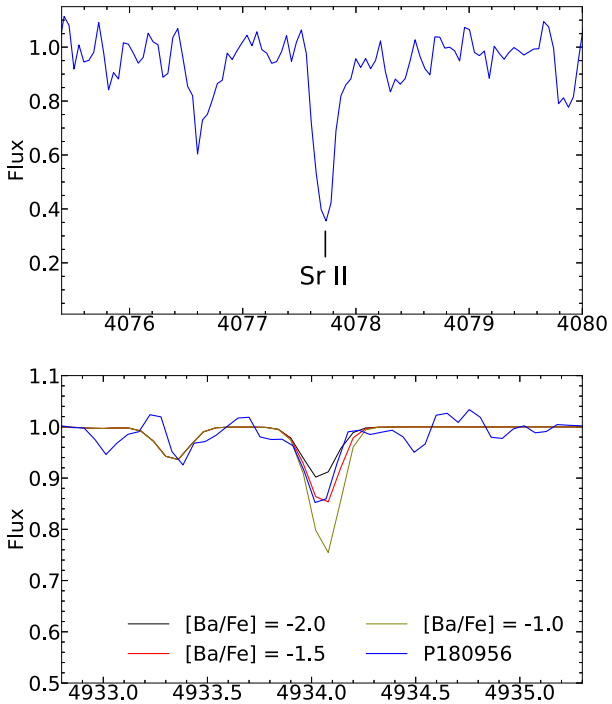

Figure 3. Sr and Ba lines. Top panel: one of the Sr lines observed in the GHOST spectrum of P180956. Bottom panel: one of the Ba lines observed is marked with a blue line, while synthetic spectra are denoted by black ([Ba/Fe] =−2.0), red ([Ba/Fe] =−1.5, best fit), and olive ([Ba/Fe] =−1.0) lines.

of GHOST and its efficiency in the blue region of the spectrum allows us to detect the two lines of Al I λλ3944.006, 3961.520 Å. K I is observable with two lines at λλ7664.899, 7698.965 Å, which are usually close to water vapour lines of the Earth's atmosphere. In this case, the K I spectral lines are well separated from the telluric lines. Sc is present with 6 Sc II lines from 4200 to 5700 Å.

4.4 Fe-peak elements

The Fe-peak elements that are observable in the GHOST spectra of this target are Fe, V, Cr, Mn, Co, Ni, Cu, and Zn (Sobeck et al. 2007; Meléndez & Barbuy 2009; Den Hartog et al. 2011; Roederer & Lawler 2012; Den Hartog et al. 2014; Lawler et al. 2014; Ruffoni et al. 2014; Wood et al. 2014; Lawler et al. 2015; Belmonte et al. 2017; Lawler et al. 2017; Wood et al. 2018; Den Hartog et al. 2019). A(Fe I) and A(Fe II) are measured from 188 and 15 lines, respectively. V I is present with the 4379.230 Å line. Cr I and Cr II are detected from eight and one line (4558.650 Å), respectively. A(Mn I) is from seven lines between 4000 and 4850 Å. A(Co I) is measured from four lines in the blue from 3800 to 4150. Ni I is detected from the λλ5476.904, 6643.630 Å lines. An upper limit on A(Cu I) is obtained with the synthesis on the λλ5105.541, 5782.132 Å lines, [Cu/Fe] <−0.2. Only line 4810.528 Å of Zn I is present in this GHOST spectrum.

4.5 Neutron-capture process elements

The blue coverage of the GHOST instrument is essential to detect the neutron-capture process elements in the spectrum of this VMP stars, namely Sr, Y, Ba, La, and Eu (Hannaford et al. 1982; Lawler et al. 2001a, b; Biémont et al. 2011; Kramida et al. 2021). Sr II is observed from the λλ4077.709, 4215.519 Å lines and it is shown in the top panel of Fig. 3. A(Y II) is measured with the SYNTH mode in MOOG

Downloaded from https://academic.oup.com/mnras/article/528/3/4838/7602409 by guest on 21 April 2024

from the λλ4398.010, 4900.119, 4883.682, 5200.409 Å, giving an upper limit of [Y/Fe] <0.0. The synthesis of Ba II is made from four lines, λλ4554.029, 4934.076, 6141.730, 6496.910 Å, which provide a value in agreement with the GRACES analysis, [Ba/Fe] ∼−1.5. The observed Ba II 4934.076 Å line and three synthetic spectra are shown in the bottom panel of Fig. 3. La II produces very weak lines, λλ4920.980, 5290.820, 5301.970, 5303.530 Å, resulting in a high upper limit, [La/Fe] <0.5. The Eu II lines, λλ4129.700, 4205.050 Å, are hard to detect, giving an upper limit of [Eu/Fe] <0.0. Other species of neutron-capture elements have been inspected, which present lines at the level of the noise, resulting in uninformative and very high upper limits.

4.6 Non-local thermodynamic equilibrium corrections

The atmosphere of VMP stars is affected by non-local thermodynamic equilibrium (NLTE) effects, which can be large for some species. NLTE corrections have been applied to Fe I and Fe II (Bergemann et al. 2012a), Mg I (Bergemann et al. 2017), Si I (Bergemann et al. 2013), Ca I (Mashonkina et al. 2017a), Ti I and Ti II (Bergemann 2011), Cr I (Bergemann & Cescutti 2010), Mn I (Bergemann et al. 2019), and Co I (Bergemann et al. 2010) using the MPIA data base.[10] For Na I (Lind et al. 2012) and Sr II (Bergemann et al. 2012b), the INSPECT[11] webtool was used. Note that NLTE corrections for Sr II are not available for a star with the stellar parameters of P180956, therefore, the closest parameters log g = 2.3 (versus 1.87 ± 0.10) and $v_{\rm micro} = 1.0\,{\rm km\,s^{-1}}$ (versus $1.5 \pm 0.1\,{\rm km\,s^{-1}}$) provide a negligible correction of ∼−0.01 dex. Similarly, Ba II NLTE corrections, adopted from Mashonkina & Belyaev (2019), are not available for this star. The closest match in their online database[12] gives a minor correction of ≲ 0.05. NLTE corrections for K are obtained from Ivanova & Shimanskiĭ (2000), which also include hyperfine structure corrections. We highlight that NLTE corrections on Fe, Ti, and Cr are helpful to obtain the ionization balance among these species, i.e. A(X I) ≈ A(X II).

Table 2 reports the chemical abundances ratios in LTE, $[X/H]_{\rm LTE}$, and $[X/Fe]_{\rm LTE}$, their uncertainties, the number of lines used, and the average NLTE corrections, $\Delta_{\rm NLTE}$.

4.7 Comparison with the GRACES spectral analysis

One of the reasons that this star P180956 was selected as a GHOST commissioning target was its unusually low [Na/Mg], [Ca/Mg], and [Ba/Fe] ratios, either in LTE or NLTE (Sestito et al. 2023a). Thus, we examine our abundance results from this improved GHOST spectrum in comparison to those from the more limited GRACES spectrum.

In general, the chemical abundance results from the GHOST spectra are similar to those from the previous GRACES analysis, as seen in Fig. 4, both in LTE. The agreement is excellent for the majority of the elements (≲ 2σ), as expected given that we have adopted the same stellar parameters. The better quality of the GHOST spectrum at all wavelengths and the larger number of lines produce a smaller line-to-line dispersion, and, therefore, smaller uncertainties on [X/H].

[10] https://nlte.mpia.de
[11] http://www.inspect-stars.com
[12] http://www.inasan.ru/~lima/pristine/ba2/

Table 2. Chemical abundances [X/H] in LTE, their final uncertainties $\sigma_{[X/H]}$, already divided by the square root of the number of lines, the [X/Fe] ratios in LTE, the number of spectral lines used $N_{\rm lines}$, and the NLTE corrections $\Delta_{\rm NLTE} = [X/H]_{\rm NLTE} - [X/H]_{\rm LTE}$.

Species	$[X/H]_{\rm LTE}$	$\sigma_{[X/H]}$	$[X/Fe]_{\rm LTE}$	$N_{\rm lines}$	$\Delta_{\rm NLTE}$
Fe I	− 1.95	0.02	–	188	+0.148
Fe II	− 1.64	0.04	–	15	+0.004
C	− 1.75	0.10	+0.20	–	–
Na I	− 2.38	0.05	− 0.43	2	− 0.457
Mg I	− 1.94	0.09	+0.01	7	+0.089
Al I	− 2.20	0.25	− 0.25	2	–
Si I	− 1.25	0.10	+0.70	1	+0.040
K I	− 1.40	0.13	+0.55	2	− 0.300
Ca I	− 2.03	0.05	− 0.08	17	+0.173
Sc II	− 1.23	0.07	+0.72	6	–
Ti I	− 1.81	0.04	+0.14	17	+0.509
Ti II	− 1.27	0.03	+0.68	30	− 0.038
V I	− 2.07	0.10	− 0.12	1	–
Cr I	− 2.23	0.04	− 0.28	8	+0.382
Cr II	− 1.87	0.10	+0.08	1	–
Mn I	− 2.40	0.05	− 0.45	7	+0.381
Co I	− 1.59	0.21	+0.36	4	+0.583
Ni I	− 1.82	0.04	+0.13	2	–
Cu I	< − 2.20	–	< − 0.25	2	–
Zn I	− 1.66	0.10	+0.29	1	–
Sr II	− 2.25	0.01	− 0.30	2	− 0.011
Y II	< − 2.00	–	< − 0.05	4	–
Ba II	− 3.50	0.10	− 1.55	4	<0.05
La II	< − 1.50	–	<+0.45	4	–
Eu II	< − 2.00	–	< − 0.05	2	–

Notes. Upper limits are expressed within 1σ.

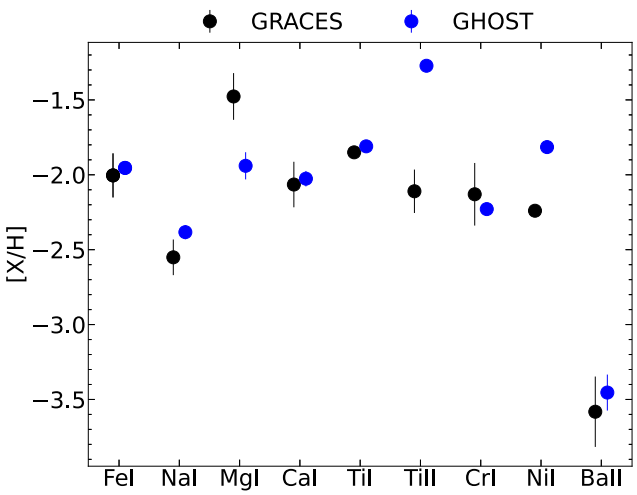

Figure 4. GHOST versus GRACES chemical abundances, [X/H]. GRACES abundances are from Sestito et al. (2023a). Both data sets are in LTE. Points are slightly offset in the horizontal direction to better show their error bars. Uncertainties on GHOST data are often smaller than the size of the marker.

Our Fe I abundance from GHOST is determined from 188 lines, whereas the GRACES analysis included only 63 lines, which improves the line-to-line scatter by a factor of ∼1.5.

Larger differences (≳ 3σ) are found for Mg I, Ti II, and Ni I. Looking at the previous analysis (Sestito et al. 2023a), this star has been analysed setting a lower metallicity value in the model

Downloaded from https://academic.oup.com/mnras/article/528/3/4838/7602409 by guest on 21 April 2024

atmosphere then the final one (by ∼0.4 dex)[13] On the other hand, EW measurements of lines in common to both analyses are similar, to within ∼5−10 percent. Hence, the former should be the main culprit to the differences we found for Mg I, Ti II, and Ni I.

4.8 Comparisons with the MW halo and bulge

The chemical abundances of P180956 are compared to a compilation of stars in the MW bulge and halo in Fig. 5. The panels in the figure are arranged in order of increasing proton number of the species. The MW bulge compilation (small light blue circles) includes results from Howes et al. (2014, 2015, 2016), Koch et al. (2016), Reggiani et al. (2020), and Lucey et al. (2022). The MW halo compilation (small grey squares) consists of stars obtained from the Stellar Abundances for Galactic Archaeology database[14] (SAGA, Suda et al. 2008), with high-resolution analysis ($R > 30\,000$), no lower or upper limits on the measurements, and low uncertainties on the chemical abundances, $\sigma_{[X/H]} < 0.2$. Both the compilations are from LTE analyses.

The chemical ratios of [Na, Mg, Ca, Sr, Ba/Fe] and upper limit for [Eu/Fe] in P180956 are situated at the lower end of the distribution observed in the MW halo and bulge. This is particularly evident for [Ba/Fe], which is nearly 2 dex lower than the majority of stars at the same [Fe/H]. In contrast, [Si, Ti, Sc, Co/Fe] ratios in P180956 are slightly enhanced compared to the literature compilations for the MW. Other upper limits (Cu, Y, and La) do not provide significant constraints on the abundances.

In the GRACES analysis (Sestito et al. 2023a), P180956 had very low [Na, Ca/Mg] ratios. Here, the revised ratios are $[Na/Mg]_{NLTE} = -0.99 \pm 0.10$ and $[Ca/Mg]_{NLTE} = -0.01 \pm 0.10$. The latter is now in line with MW halo and DGs expectations (e.g. Hansen et al. 2020; Ji et al. 2020). Comparing the other α −elements to Mg, this star shows $[Si/Mg]_{NLTE} = +0.64 \pm 0.10$ and $[Ti/Mg]_{NLTE} = +0.55 \pm 0.10$. Thus, P180956 exhibits very low [Na/Fe], slightly sub-solar [Mg, Ca/Fe], enhanced [Si, Ti/Mg], in addition to a very low Ba-content. This is a somewhat unusual chemical abundance pattern for a typical MW halo or bulge star.

5 GALACTIC ORBIT

Orbital parameters are derived using GALPY code (Bovy 2015), integrating the orbit for 1 Gyr in the future and in the past. Uncertainties are determined through a Monte Carlo simulation (1000 iterations) on the input quantities, drawn from a Gaussian distribution. Two Galactic gravitational potentials are adopted and the relative orbits are displayed in Fig. 6. One potential corresponds to the model used in Sestito et al. (2023a), which includes a rotating bar (black line); the second (blue line) is without the bar as in Sestito et al. (2019). These two gravitational potentials lead to a very similar orbit.

In both cases, P180956 exhibits a slightly prograde orbit (vertical angular momentum $L_z \sim 300$ kpc km s^{-1}), which is confined to the MW plane ($Z_{max} \sim 2$ kpc). The pericentric ($R_{peri} \sim 0.7$ kpc) and apocentric ($R_{apo} \sim 13$ kpc) distances indicate that the star's trajectory takes it very close to the Galactic Centre before venturing far beyond the Sun's position, resulting in an orbit characterized by high eccentricity ($\epsilon \sim 0.9$). These results are in agreement within 1σ with the previous orbital analysis from Sestito et al. (2023a).

Table 3 reports pericentric and apocentric distances, the eccentricity, the maximum excursion from the plane, the vertical component of the angular momentum as calculated using both gravitational potentials.

6 DISCUSSION

P180956 has peculiar kinematics that indicate that the star is confined to the MW plane on a very eccentric orbit, reaching both the very inner region of the MW and a position well beyond the Sun (see Fig. 6).

Furthermore, P180956 showed a very low amount of [Ba/Fe], [Ca/Mg], and [Na/Mg]. These signatures stand out when compared to MW halo stars, and resemble the abundances of stars found at present in UFD galaxies. Low chemical abundance ratios in the elements listed above have been interpreted as a sign of contributions from a small number of low-mass supernovae type II (SNe II) in the past, for example, the so called 'one-shot' model (Frebel et al. 2010a). Therefore, the interpretation of the chemo-dynamical properties from the GRACES spectrum implied that this star may have formed in an ancient DG accreted very early in the MW formation. In the following subsections, a revised and more thorough discussion on the origin of this star and on the properties of its formation site is presented.

6.1 The yields of the supernovae progenitors

The wavelength coverage of GHOST and the SNR of the observed spectra allow the detection of up to 18 chemical species and four meaningful upper limits, for a total of 13 elements beyond those available in the previous GRACES spectral analysis. Comparing this extensive set of chemical abundances with the predicted yields of supernovae from theoretical models can be used for insights into the nucleosynthetic processes that occurred at the formation site of P180956. To accomplish this, the online tool STARFIT[15] is used. The yields of best fit are obtained by combining the type II supernovae yields of the best solutions chosen from a pool of theoretical models. A total of ten models have been selected, encompassing various types of supernovae events, i.e. hypernovae, core-collapse, rotating massive stars, neutron stars mergers, and pair-instability SNe.

The theoretical yields [X/H] from contributing SNe are compared with the observational data in the top panel of Fig. 7. The scaled solar abundances ratios (black line) are from Asplund et al. (2009), shifted to match the [Fe/H] of P180956. These fail to reproduce our data, except for Fe (by design), Na, and Mg. The solar abundances pattern predicts a net decrease in the yields from Si, which is not seen in P180956.

The best-fitting solution (magenta line) from STARFIT consists in five SNe II events originating from Population III stars. This fit is a mixture of three low-mass hypernovae[16] with $M \sim 10\,M_\odot$ (Heger & Woosley 2010; Heger et al. 2012), one around $M \sim 15\,M_\odot$ (Limongi & Chieffi 2018), and one intermediate-mass ($\sim 80\,M_\odot$) fast-rotating (~ 300 km s^{-1}) supernova (Grimmett et al. 2018). The second best-fitting (orange line) solution is composed of three events, two low-mass hypernovae with $M \sim 10-17\,M_\odot$ (Heger & Woosley 2010; Heger et al. 2012) and one fast-rotating (~ 300 km s^{-1}) SN with $M \sim 120\,M_\odot$ (Limongi & Chieffi 2018).

The difference between the observed [X/H] and the theoretical yields from the best (magenta circles) and second best (orange

[13]We reassure the reader that this is the only star in Sestito et al. (2023a) for which the model atmosphere was not updated to the final value.
[14]http://sagadatabase.jp

[15]https://starfit.org
[16]A hypernova explosion has a typical energy of at least a factor of ∼10 greater than a classical supernova type II.

Downloaded from https://academic.oup.com/mnras/article/528/3/4838/7602409 by guest on 21 April 2024

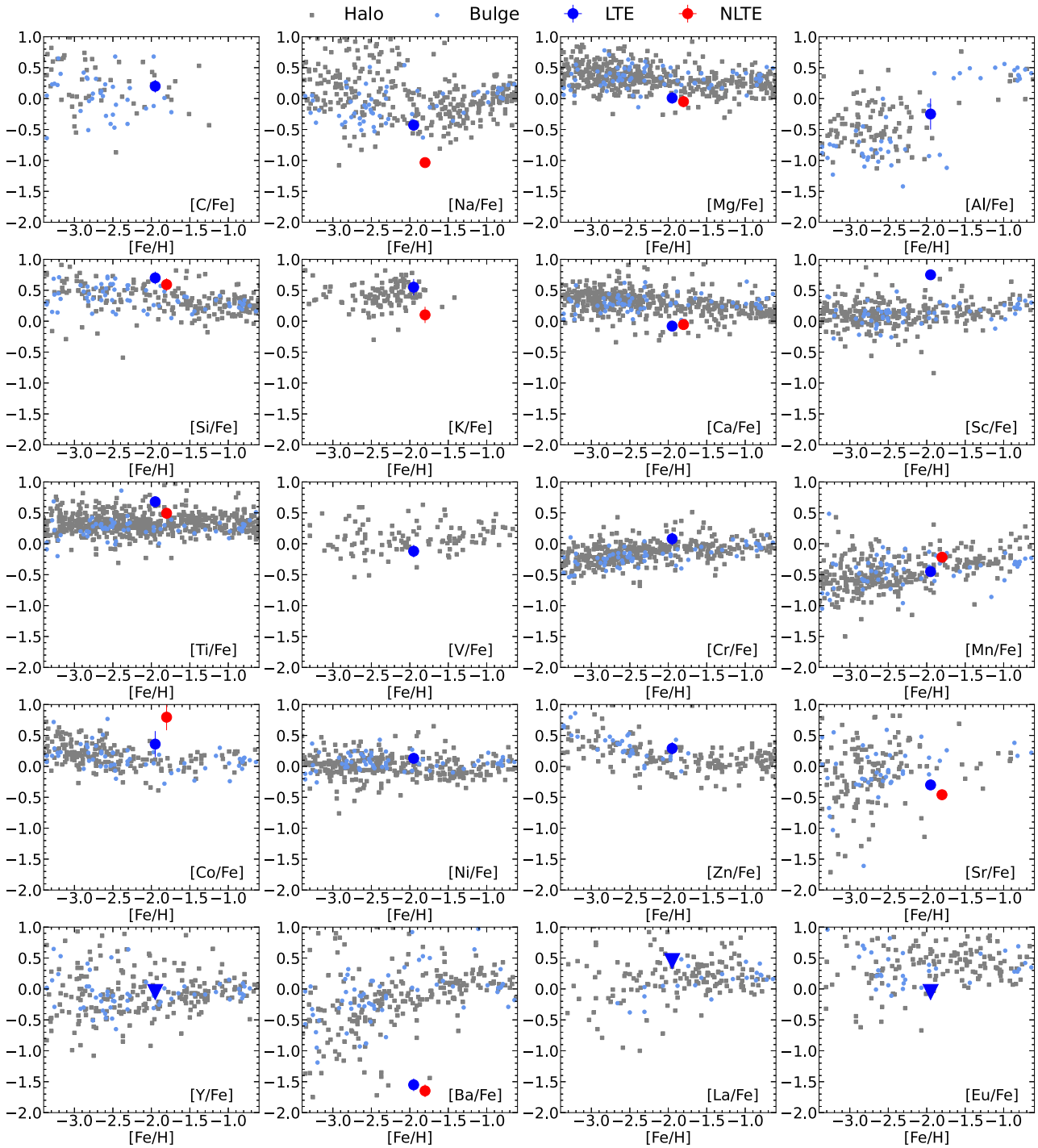

Figure 5. Chemical abundances. Blue and red circles represent the chemical abundances of P180956 in LTE and NLTE corrected, respectively. Blue triangles denote upper limits for P180956. Small light blue circles represent the bulge compilation (Howes et al. 2014, 2015, 2016; Koch et al. 2016; Reggiani et al. 2020; Lucey et al. 2022), while small grey squares correspond to the halo compilation from the SAGA database (Suda et al. 2008). The uncertainties on [X/Fe] for P180956 are often smaller than the symbol size. The scarcity of literature stars in the [K/Fe] panel may be attributed to the difficulty in measuring K spectral lines in the optical range, as they can be blended with telluric water vapour lines.

squares) fits are displayed in the bottom panel of Fig. 7. Both solutions provide a difference below $\lesssim 0.3$ in absolute value for the majority of the species.

We want to emphasise that the use of StarFit is more as an illustration of the range of events that might be needed to explain the chemistry of this star. StarFit suggests an interpretation that contributions from high-mass supernovae ($> 140\,M_\odot$, e.g. pair instability) and neutron-star mergers are ruled out for this star. The former would produce a strong odd–even effect in the yields (Takahashi et al. 2018; Salvadori et al. 2019), i.e. very low [Na, Al/Mg] (~ -1.3) and

Downloaded from https://academic.oup.com/mnras/article/528/3/4838/7602409 by guest on 21 April 2024

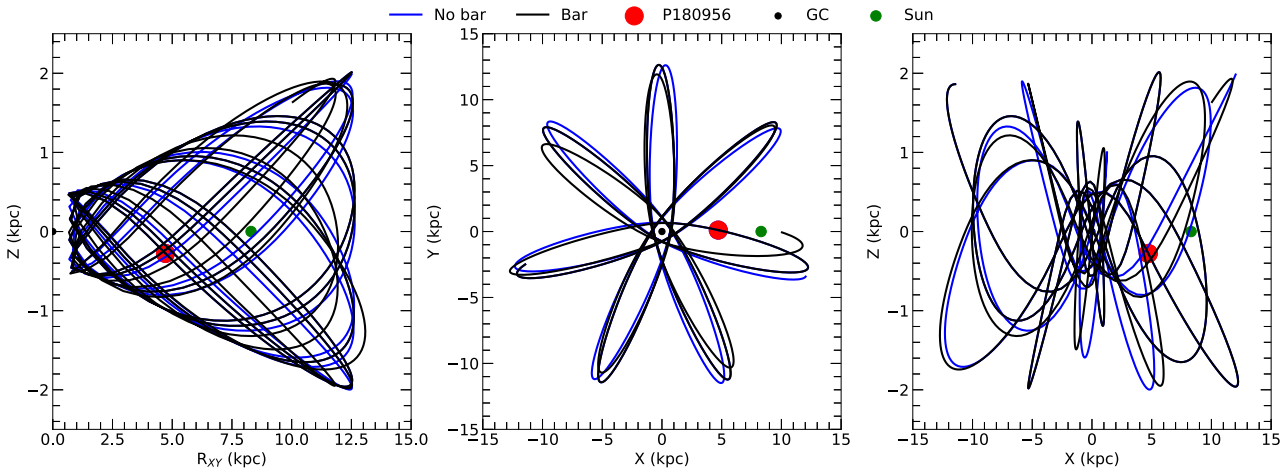

Figure 6. Galactic orbit of P180956. Left panel: height from the plane Z versus in-plane projected distance R_{XY}. Central panel: Y versus X Galactic positions. Right panel: Z versus X Galactic positions. Black and blue lines represent the orbit integrated in a gravitational potential with and without the presence of a rotating bar as in Sestito et al. (2023a) and as in Sestito et al. (2019), respectively. The red, black, and green circles mark the position of P180956, of the Galactic Centre (GC), and of the Sun at the present-day.

Table 3. Pericentric and apocentric distances (R_{peri}, R_{apo}), the eccentricity (ϵ), the maximum excursion from the plane (Z_{max}), and the vertical component of the angular momentum (L_z) are reported.

Quantity	Bar	No bar
R_{peri} (kpc)	0.67 ± 0.21	0.73 ± 0.18
R_{apo} (kpc)	12.82 ± 1.06	12.67 ± 0.74
ϵ	0.90 ± 0.03	0.89 ± 0.02
Z_{max} (kpc)	2.01 ± 0.35	2.02 ± 0.33
L_z (kpc km s^{-1})	307.0 ± 83.0	303.0 ± 85.0

high [Ca/Mg] ($\gtrsim +0.6$); the latter would produce an enrichment in neutron-capture elements (e.g. Cowan et al. 2021). Both scenarios are in contrast with the observed chemical properties of P180956. StarFit suggests that the main contributing SNe II are in the low-mass range. Specifically, hypernovae are necessary to produce the high [Si, Ti/Mg] ratios, and they provide a little contribution to heavy elements. These findings align with the scenario proposed by Ishigaki et al. (2018), where low-mass hypernovae ($\lesssim 40\,M_\odot$) are the primary sources of enrichment of the interstellar medium during the early stages of chemical evolution. In addition, the presence of one fast-rotating intermediate-mass supernova is needed to well reproduce the pattern of the heavy elements, i.e. Sr and Ba.

6.2 *In situ* versus accreted diagnostics

What if this star formed *in situ*, i.e. in the protodisc but after the early Galactic assembly? The period between the early MW assembly and the formation of the disc, dubbed 'Aurora' (Belokurov & Kravtsov 2022), has been proposed to be very chaotic, forming bound massive clusters, chemically similar to GCs (Belokurov & Kravtsov 2023). This implies that some Aurora stars would be enriched in N, Na, and Al, while others would resemble the 'normal' halo stars (Belokurov & Kravtsov 2023). P180956 is Na-poor, Al-normal, and neutron-capture process poor, with the latter being very rare for halo stars at that metallicity (see Fig. 5). This chemical pattern rules out the 'Aurora' as the origin for P180956.

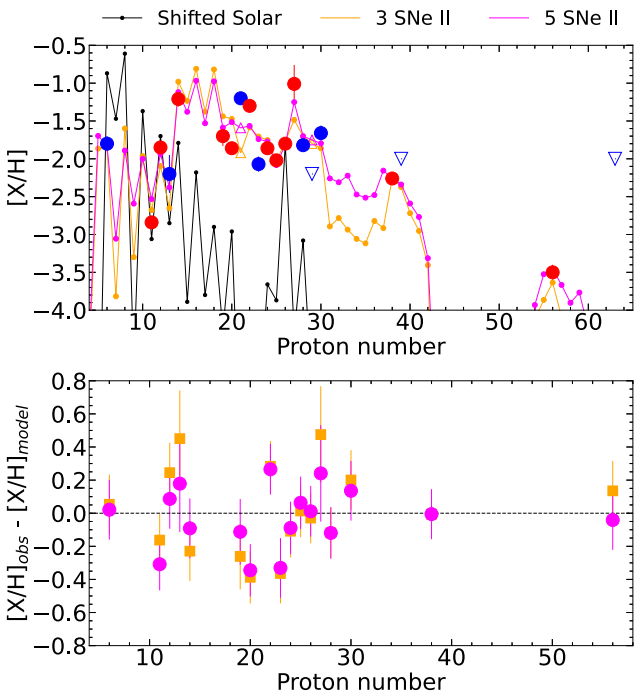

Figure 7. Supernovae yields. Red and blue circles are NLTE and LTE [X/H] of P180956, respectively. Upper limits of Cu, Y, and Eu are marked with empty downward blue triangles. Top panel: black dots and line represent the solar-scaled abundances from Asplund et al. (2009) shifted to match the [Fe/H] of P180956. Magenta and orange dots and lines represent the theoretical yields from the best (five SNe II events) and second best fit (three SNe II events), respectively. Lower limits of Sc and Cu in the theoretical models are denoted with empty upward triangles. Bottom panel: the difference between the observed [X/H] and the yields predicted by the best (magenta circles) and second best (orange squares) fit from StarFit. Upper limits in the data and lower limits in the modelled yields are removed. Uncertainties on the data are summed in quadrature to 0.15 for the theoretical yields. The horizontal dashed line marks the null difference.

Downloaded from https://academic.oup.com/mnras/article/528/3/4838/7602409 by guest on 21 April 2024

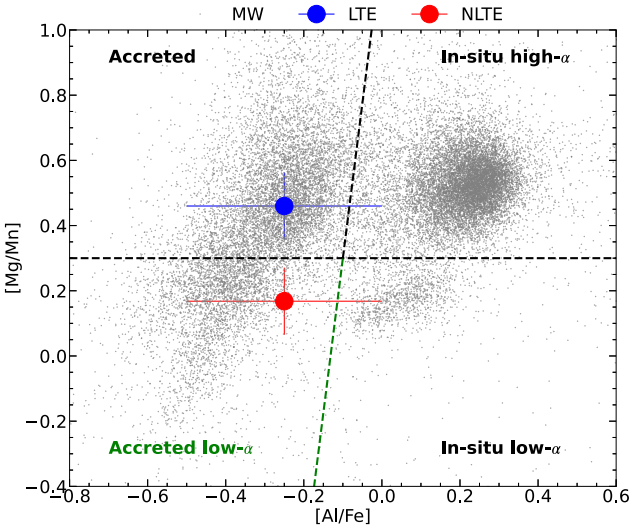

Figure 8. [Mg/Mn] versus [Al/Fe] space. P180956 data are shown in blue and red in LTE and NLTE-corrected ([Mg/Mn] only), respectively. Small grey dots are APOGEE DR17 MW stars selected to have SNR >70 and [Fe/H] < −0.7, which are derived from an NLTE analysis. The three regions delimited by the dashed black lines, accreted and *in situ* low-/high-α are defined following Das et al. (2020) and Horta et al. (2021). The accreted region has been prolonged following the dashed green line, in which accreted low-α stars should lie.

Other studies have suggested [Mg/Mn] versus. [Al/Fe] as a diagnostic to differentiate accreted stars from *in situ* stars (e.g. Das et al. 2020; Horta et al. 2021). Fig. 8 illustrates this chemical space, including APOGEE DR17 (Abdurro'uf et al. 2022) stars for comparison. Dashed black lines delineate three regions where accreted, *in situ* low-α, and *in situ* high-α stars are more likely to be found (e.g. Das et al. 2020; Horta et al. 2021). In the LTE case, P180956 lies close to the centre of the accreted 'blob', while considering NLTE corrections, the star falls into the *in situ* low-α region.

Recently, Horta et al. (2023) provide a summary of the chemo-dynamical properties of known accreted structures based on the latest Gaia and APOGEE data releases. Their fig. 13 displays the [Mg/Mn] versus [Al/Fe] space for all the accreted known structures, showing that some of their stars have [Mg/Mn] ∼0.0 or even negative [e.g. Sagittarius, Sequoia, Gaia–Sausage–Enceladus (GSE)]. Therefore, part of the *in situ* low-α region, is actually accreted. The accreted region in Fig. 8 is here tentatively extended (accreted low α), by lengthening the dashed-green line, which suggests that P180956 is of accreted origin. Offsets between the NLTE infrared (APOGEE) and the NLTE-corrected optical analyses are estimated to be Δ[Mg/Mn] = +0.15 ± 0.18 and Δ[Al/Fe] = −0.11 ± 0.12 (Jönsson et al. 2020). These corrections, not applied in Fig. 8, would move P180956 more closely to the accreted low-α 'blob'.

Can P180956 be associated with any of the recently discovered accreted structures? The system that bears the closest resemblance to P180956 in terms of kinematical properties (see Horta et al. 2023) is GSE (e.g. Belokurov et al. 2018; Helmi et al. 2018). The high eccentric orbit of GSE (0.93 ± 0.06) and its mean pericentric and apocentric distances ($r_{\rm peri}$ = 0.61 ± 1.03 kpc and $r_{\rm apo}$ = 17.15 ± 5.22 kpc) are compatible with P180956's orbital parameters within 1σ (see Table 3). However, stars of GSE reach a maximum height from the plane that is typically greater than the one of our target ($Z_{\rm max}$ = 9.84 ± 6.14 kpc versus $Z_{\rm max}$ = 2.01 ± 0.35 kpc).

Helmi et al. (2018) demonstrate that the GSE population has lower [α/Fe] ratios compared to stars in the MW halo. Similarly, Hayes et al. (2018) provide evidence for a low-α population, showing that its stars exhibit [Mg, Si/Fe]$_{\rm NLTE}$ ∼ 0.25−0.30 at the [Fe/H] of P180956. However, these ratios are not compatible with the values of our target, which have [Mg/Fe]$_{\rm NLTE}$ = −0.05 ± 0.09 and [Si/Fe]$_{\rm NLTE}$ = +0.59 ± 0.10. Thus, the chemo-dynamical properties of P180956 differ from those of GSE and other known accreted structures.

6.3 Origin in an ultrafaint dwarf galaxy

A comparison of the neutron-capture elements [Sr/Fe] and [Ba/Fe] versus. [Fe/H] for P180956, stars from UFDs, from classical DGs, and MW halo is presented in the left panels of Fig. 9. It is evident that P180956 exhibits lower [Sr, Ba/Fe] (and [Eu/Fe] from Fig. 5) ratios than the majority of MW halo stars at the same metallicity. The [Sr/Fe] of P180956 is similar to the bulk value of DGs, while UFDs have lower values. On the opposite behaviour is [Ba/Fe], where P180956's ratio is similar to those in the low-end distribution of UFDs. The low-abundance of neutron-capture processes elements has been interpreted as the contribution of low-mass supernovae and the absence of neutron stars mergers events (e.g. Cowan et al. 2021). Furthermore, the combinations of stochasticity in the production of neutron-capture elements with the inability of UFDs to retain metals can explain the low [Sr, Ba, Eu/Fe] observed in these systems (e.g. Venn et al. 2012; Ji et al. 2019).

The distribution of [Sr/Ba] versus [Ba/Fe] is shown in the right panel of Fig. 9. Halo stars exhibit a downward trend as [Ba/Fe] increases (Mashonkina et al. 2017b), albeit mostly clumped around [Sr/Ba] ∼0.3 (Ji et al. 2019). Both UFDs and DGs present a wide distribution in [Sr/Ba] (up to ∼1.5 dex), with UFDs populate a distinct region from the majority of MW halo stars and of DGs (Roederer 2017; Mashonkina et al. 2017b; Ji et al. 2019; Reichert et al. 2020; Sitnova et al. 2021). P180956 has a relatively high [Sr/Ba] ratio, close to the upper-end of the distributions of the MW halo, Coma Berenices (UFD), and Sculptor (DG), while its [Ba/Fe] is typical of a UFD's star.

Did this star originate in a UFD or in classical DG? At the metallicity of P180956, DGs would likely involve contributions from asymptotic giant branch stars (AGBs) and, in some cases, SNe Ia (see de los Reyes et al. 2020; Sestito et al. 2023b, for Sculptor and Ursa Minor). AGBs would produce Ba via s-process nucleosynthesis (e.g. Pignatari et al. 2008; Cescutti & Chiappini 2014), reaching solar values. Additional contribution from SNe Ia would lower the overall [α/Fe] ratios to solar or sub-solar values. Given P180956 has a very low-Ba ([Ba/Fe]$_{\rm NLTE}$ ∼ −1.7) and the inhomogeneity in the α-elements ([Si, Ti/ Mg, Ca] ∼0.5), the contributions of AGBs and SNe Ia are likely ruled out, and, as well, the DG scenario.

How to explain the high [Sr/Ba]? Mashonkina et al. (2017b) discuss that sub-solar [Sr/Ba] implies that both elements are produced solely by r-process, while solar- and supersolar-[Sr/Ba] indicate the involvement of s-processes in the Sr production. Various kinds of supernovae events have been proposed to explain the relative excess of Sr compared to other neutron-capture elements (Mashonkina et al. 2017b, and references therein). Hypernovae (Izutani et al. 2009) and s-process nucleosynthesis in low-metallicity fast-rotating supernovae (Pignatari et al. 2008; Banerjee et al. 2018; Grimmett et al. 2018; Limongi & Chieffi 2018) are also listed among these, which are always invoked by the best-fitting models from StarFit (see Section 6.1). We note from StarFit that the fast-rotating supernova is the event the contribute most to the [Sr/Ba] enrichment.

Downloaded from https://academic.oup.com/mnras/article/528/3/4838/7602409 by guest on 21 April 2024

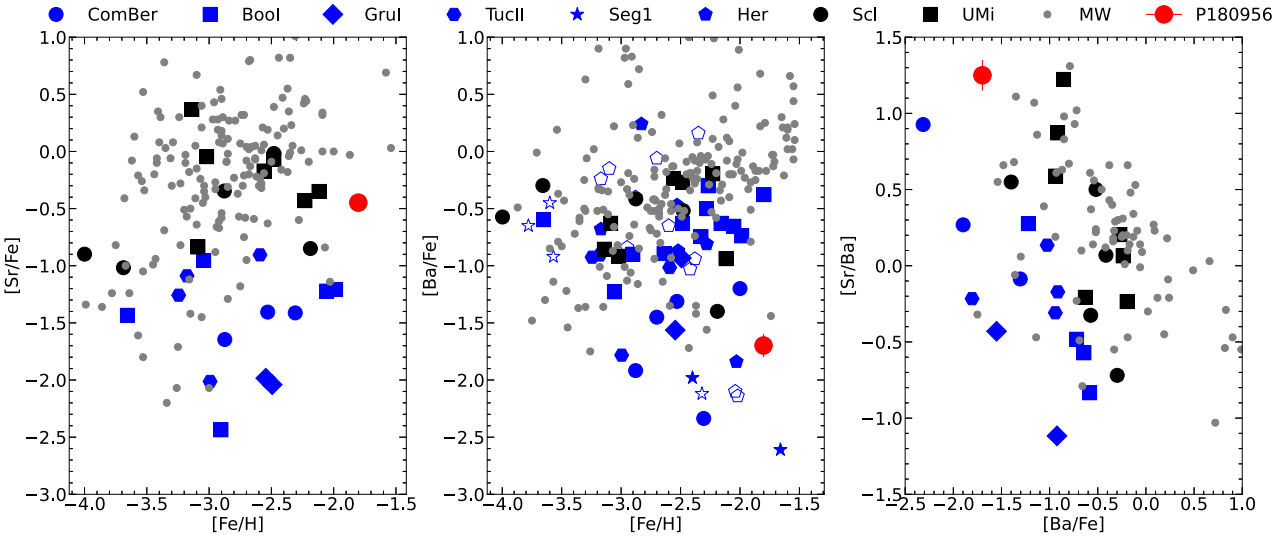

Figure 9. Neutron-capture elements. Left panel: [Sr/Fe] versus [Fe/H]. Central panel: [Ba/Fe] versus [Fe/H]. Empty symbols denote upper limits on the vertical axis. Right panel: [Sr/Ba] versus [Ba/Fe]. The red circle marks the NLTE-corrected chemical ratios of P180956. MW stars are from the SAGA database (Suda et al. 2008); Coma Berenice (ComBer) stars are from Frebel et al. (2010b) and Waller et al. (2023); Bootes I (BooI) stars are from Feltzing et al. (2009), Norris et al. (2010), Gilmore et al. (2013), Ishigaki et al. (2014), and Frebel et al. (2016); Gru I stars are from Ji et al. (2019); Tucana II (TucII) stars are from Ji et al. (2016) and Chiti et al. (2018); Segue 1 (Seg1) stars are from Frebel et al. (2014); Hercules (Her) stars are from Koch et al. (2008), Koch et al. (2013), and François et al. (2016); Sculptor (Scl) and Ursa Minor (UMi) stars are from Mashonkina et al. (2017b).

6.4 P180956, witness of the early Galactic assembly

Above we have outlined the most likely origin for P180956 as from an accreted UFD. Two new questions now arise whether the star was brought in during the early Galactic assembly or later on and if its system was isolated or brought in with one of the massive known accreted satellites.

P180956 was also selected for GHOST commissioning because of its peculiar orbital parameters, as it remains relatively close to the MW plane (see Fig. 6). Recently, the presence of this population has been observed from the ultra metal-poor regime ([Fe/H] ≤ -4.0, Sestito et al. 2019) to the disc's metallicity (Di Matteo et al. 2020; Sestito et al. 2020; Venn et al. 2020; Cordoni et al. 2021; Mardini et al. 2022), finding that the majority of them moves in a prograde orbit. While VMP 'planar' stars have been dynamically detected in various investigations, thorough and detailed analyses of their chemical properties are scarce.

The existence of this population has also been explored through high-resolution cosmological zoom-in simulations (Santistevan et al. 2021; Sestito et al. 2021). The simulations[17] predict the presence of a 'planar' population. While previous observational studies focused on the origin of low-eccentricity stars, Sestito et al. (2021) also discussed that the more eccentric members of the planar population are likely brought in during the early-assembly phase. This is because, during that epoch, the gravitational potential of the forming proto-Galaxy is still shallow, allowing for the deposit of accreted systems into the inner regions. The relatively small excursion from the MW plane, the pericentric and apocentric distances, in addition to the high eccentricity suggest that the star was brought in during the early-assembly phase.

[17]Sestito et al. (2021) utilized the NIHAO-UHD simulations (Buck et al. 2019), while Santistevan et al. (2021) employed the FIRE simulations (Hopkins et al. 2018).

In Section 6.2, we rule out that P180956 formed in one of the known accreted structures, however, given (1) that some of its orbital parameters are similar to those of GSE (except for Z_{max}), (2) its formation likely in a UFD-like system (see Section 6.3), and (3) its early accretion to the MW, two scenarios on the origin of P180956 are proposed. The first is that P180956 originate in one of the many low-mass building blocks that formed the proto-MW, which had chemical and physical properties similar to those of present UFDs; the second is that its progenitor system was a UFD satellite of GSE, that has been brought in into the inner Galaxy during the infall of GSE.

7 CONCLUSIONS

This work represents the second high-resolution spectroscopic analysis utilizing the GHOST spectrograph mounted at Gemini South, following the detailed analysis of two r-process rich stars in the Reticulum II UFD galaxy (Hayes et al. 2023). The spectra of P180956, a star with unique chemo-dynamical properties, were observed during the second commissioning run of the instrument in September 2022. Previously, the star was observed with GRACES at Gemini North and analysed as part of the PIGS (Arentsen et al. 2020a; Sestito et al. 2023a). In this study, we conducted a comprehensive analysis of the chemo-dynamical properties of P180956, leading to the following results:

(i) The high efficiency and wide spectral coverage of the GHOST instrument (see Fig. 1) enabled the detection of approximately 20 atomic species (see Fig. 5), which is almost twice than what was possible to measure with GRACES (Kielty et al. 2021; Jeong et al. 2023; Waller et al. 2023; Sestito et al. 2023a, b). These species provide crucial insights into the origin and chemical properties of P180956 and its formation site.

(ii) Theoretical models of supernovae yields suggest that the formation site of P180956 experienced pollution from 2 to 4 low-mass hypernovae ($\lesssim 15\,M_{\odot}$) and one intermediate-

Downloaded from https://academic.oup.com/mnras/article/528/3/4838/7602409 by guest on 21 April 2024

mass ($80-120\,M_\odot$) fast-rotating ($\sim 300\,\mathrm{km\,s^{-1}}$) supernova (see Fig. 7).

(iii) These combinations of supernovae events resulted in a composition of α-elements with solar Ca and Mg abundances and enhanced Si and Ti abundances (see Figs 5 and 7).

(iv) The specific combination of supernovae yields led to low abundances of neutron-capture elements (Sr, Ba, and Eu), with a relatively high [Sr/Ba] ratio (see Fig. 9). This can be explained with the additional s-process channels for Sr production that occur mostly in fast-rotating supernovae.

(v) The kinematical properties of P180956 (see Fig. 6) suggest the star was likely accreted during the early-assembly phase of the MW. Its [Mg/Mn] ratio is also indicative of its accreted origin (see Fig. 8).

(vi) None of the known accreted structures exhibit chemo-dynamical properties resembling perfectly those of P180956. Only GSE has similar eccentricity, apocentric and pericentric distances to P180956.

(vii) P180956 originated in an ancient system chemically similar to present UFD galaxies, given the low amount of neutron-capture elements (see Figs 5 and 9), either accreted alone or dragged in with GSE as its satellite.

The advent of the GHOST high-resolution spectrograph has been invoked by various chemo-dynamical investigations targeting the MW and its satellite systems (e.g. Waller et al. 2023; Sestito et al. 2023a, b). This study, along with Hayes et al. (2023) and Dovgal et al. (2024), demonstrates that the combination of the Gemini South's large aperture and GHOST's high efficiency and wide spectral coverage is ideal for investigating low-metallicity stars in the MW and nearby systems. The synergy between GHOST and the Gaia satellite will undoubtedly propel Galactic Archaeological studies forward.

ACKNOWLEDGEMENTS

We acknowledge and respect the lək̓ʷəŋən peoples on whose traditional territory the University of Victoria stands and the Songhees, Esquimalt and W̱SÁNEĆ peoples whose historical relationships with the land continue to this day.

We thank the anonymous referee for their insightful comments, which improved the quality of the manuscript.

FS thanks the Dr Margaret 'Marmie' Perkins Hess postdoctoral fellowship for funding his work at the University of Victoria. KAV thanks the National Sciences and Engineering Research Council of Canada for funding through the Discovery Grants and CREATE programs. AA-A acknowledges support from the Herchel Smith Fellowship at the University of Cambridge and a Fitzwilliam College research fellowship supported by the Isaac Newton Trust. NFM gratefully acknowledges support from the French National Research Agency (ANR) funded project 'Pristine' (ANR-18-CE31-0017) along with funding from the European Research Council (ERC) under the European Unions Horizon 2020 research and innovation programme (grant agreement no. 834148). TM acknowledges the Spinoza Grant from the Dutch Research Council (NWO) for supporting his research. ES acknowledges funding through VIDI grant 'Pushing Galactic Archaeology to its limits' (with project number VI.Vidi.193.093) which is funded by the Dutch Research Council (NWO). This research was supported by the International Space Science Institute (ISSI) in Bern, through ISSI International Team project 540 (the early Milky Way).

This work is based on observations obtained with Gemini South/GHOST, during the commissioning run of 2022 September. Based on observations obtained at the international Gemini Observatory, a program of NSF's NOIRLab, which is managed by the Association of Universities for Research in Astronomy (AURA) under a cooperative agreement with the National Science Foundation. On behalf of the Gemini Observatory partnership: the National Science Foundation (United States), National Research Council (Canada), Agencia Nacional de Investigación y Desarrollo (Chile), Ministerio de Ciencia, Tecnología e Innovación (Argentina), Ministério da Ciência, Tecnologia, Inovações e Comunicações (Brazil), and ⟨0:funding-source 3:href="http://dx.doi.org/10.13039/501100003717"⟩Korea Astronomy and Space Science Institute⟨/0:funding-source⟩ (Republic of Korea).

This work has made use of data from the European Space Agency (ESA) mission *Gaia* (https://www.cosmos.esa.int/gaia), processed by the *Gaia* Data Processing and Analysis Consortium (DPAC, https://www.cosmos.esa.int/web/gaia/dpac/consortium). Funding for the DPAC has been provided by national institutions, in particular, the institutions participating in the *Gaia* Multilateral Agreement.

This research has made use of the SIMBAD database, operated at CDS, Strasbourg, France (Wenger et al. 2000). This work made extensive use of TOPCAT (Taylor 2005).

DATA AVAILABILITY

The data underlying this article are available in the paper and in its online supplementary material.

REFERENCES

Abadi M. G., Navarro J. F., Steinmetz M., Eke V. R., 2003, ApJ, 597, 21
Abdurro'uf et al., 2022, ApJS, 259, 35
Aguado D. S. et al., 2019, MNRAS, 490, 2241
Arentsen A. et al., 2020a, MNRAS, 491, L11
Arentsen A. et al., 2020b, MNRAS, 496, 4964
Asplund M., Grevesse N., Sauval A. J., Scott P., 2009, ARA&A, 47, 481
Banerjee P., Qian Y.-Z., Heger A., 2018, ApJ, 865, 120
Beasley M. A., Leaman R., Gallart C., Larsen S. S., Battaglia G., Monelli M., Pedreros M. H., 2019, MNRAS, 487, 1986
Belmonte M. T., Pickering J. C., Ruffoni M. P., Den Hartog E. A., Lawler J. E., Guzman A., Heiter U., 2017, ApJ, 848, 125
Belokurov V., Kravtsov A., 2022, MNRAS, 514, 689
Belokurov V., Kravtsov A., 2023, MNRAS, 525, 4456
Belokurov V., Erkal D., Evans N. W., Koposov S. E., Deason A. J., 2018, MNRAS, 478, 611
Bensby T. et al., 2013, A&A, 549, A147
Bensby T. et al., 2017, A&A, 605, A89
Bergemann M., 2011, MNRAS, 413, 2184
Bergemann M., Cescutti G., 2010, A&A, 522, A9
Bergemann M., Pickering J. C., Gehren T., 2010, MNRAS, 401, 1334
Bergemann M., Lind K., Collet R., Magic Z., Asplund M., 2012a, MNRAS, 427, 27
Bergemann M., Hansen C. J., Bautista M., Ruchti G., 2012b, A&A, 546, A90
Bergemann M., Kudritzki R.-P., Würl M., Plez B., Davies B., Gazak Z., 2013, ApJ, 764, 115
Bergemann M., Collet R., Amarsi A. M., Kovalev M., Ruchti G., Magic Z., 2017, ApJ, 847, 15
Bergemann M. et al., 2019, A&A, 631, A80
Bessell M., Bloxham G., Schmidt B., Keller S., Tisserand P., Francis P., 2011, PASP, 123, 789
Biémont É. et al., 2011, MNRAS, 414, 3350
Bovy J., 2015, ApJS, 216, 29

Downloaded from https://academic.oup.com/mnras/article/528/3/4838/7602409 by guest on 21 April 2024

Buck T., Obreja A., Macciò A. V., Minchev I., Dutton A. A., Ostriker J. P., 2019, MNRAS, 525, 4456
Bullock J. S., Johnston K. V., 2005, ApJ, 635, 931
Cescutti G., Chiappini C., 2014, A&A, 565, A51
Chene A.-N. et al., 2014, in Navarro R., Cunningham C. R., Barto A. A.eds, SPIE Conf. SeriesVol. 9151, Advances in Optical and Mechanical Technologies for Telescopes and Instrumentation. SPIE, Bellingham. p. 915147
Chiti A., Frebel A., Ji A. P., Jerjen H., Kim D., Norris J. E., 2018, ApJ, 857, 74
Cordoni G. et al., 2021, MNRAS, 503, 2539
Cowan J. J., Sneden C., Lawler J. E., Aprahamian A., Wiescher M., Langanke K., Martínez-Pinedo G., Thielemann F.-K., 2021, Rev. Mod. Phys., 93, 015002
Das P., Hawkins K., Jofré P., 2020, MNRAS, 493, 5195
de los Reyes M. A. C., Kirby E. N., Seitenzahl I. R., Shen K. J., 2020, ApJ, 891, 85
Den Hartog E. A., Lawler J. E., Sobeck J. S., Sneden C., Cowan J. J., 2011, ApJS, 194, 35
Den Hartog E. A., Ruffoni M. P., Lawler J. E., Pickering J. C., Lind K., Brewer N. R., 2014, ApJS, 215, 23
Den Hartog E. A., Lawler J. E., Sneden C., Cowan J. J., Brukhovesky A., 2019, ApJS, 243, 33
Den Hartog E. A., Lawler J. E., Sneden C., Cowan J. J., Roederer I. U., Sobeck J., 2021, ApJS, 255, 27
Den Hartog E. A., Lawler J. E., Sneden C., Roederer I. U., Cowan J. J., 2023, ApJS, 265, 42
Di Matteo P., Spite M., Haywood M., Bonifacio P., Gómez A., Spite F., Caffau E., 2020, A&A, 636, A115
Dovgal A. et al., 2024, MNRAS, 527, 7810
El-Badry K. et al., 2018, MNRAS, 480, 652
Evans D. W. et al., 2018, A&A, 616, A4
Feltzing S., Eriksson K., Kleyna J., Wilkinson M. I., 2009, A&A, 508, L1
François P., Monaco L., Bonifacio P., Moni Bidin C., Geisler D., Sbordone L., 2016, A&A, 588, A7
Frebel A., Kirby E. N., Simon J. D., 2010a, Nature, 464, 72
Frebel A., Simon J. D., Geha M., Willman B., 2010b, ApJ, 708, 560
Frebel A., Simon J. D., Kirby E. N., 2014, ApJ, 786, 74
Frebel A., Norris J. E., Gilmore G., Wyse R. F. G., 2016, ApJ, 826, 110
Freeman K., Bland-Hawthorn J., 2002, ARA&A, 40, 487
Gilmore G., Norris J. E., Monaco L., Yong D., Wyse R. F. G., Geisler D., 2013, ApJ, 763, 61
González Hernández J. I., Bonifacio P., 2009, A&A, 497, 497
Green G. M., Schlafly E., Zucker C., Speagle J. S., Finkbeiner D., 2019, ApJ, 887, 93
Grimmett J. J., Heger A., Karakas A. I., Müller B., 2018, MNRAS, 479, 495
Gustafsson B., Edvardsson B., Eriksson K., Jørgensen U. G., Nordlund Å., Plez B., 2008, A&A, 486, 951
Hannaford P., Lowe R. M., Grevesse N., Biemont E., Whaling W., 1982, ApJ, 261, 736
Hansen T. T. et al., 2020, ApJ, 897, 183
Hayes C. R. et al., 2018, ApJ, 852, 49
Hayes C. R. et al., 2022, in Evans C. J., Bryant J. J., Motohara K.eds, SPIE Conf. Ser.Vol. 12184, Ground-based and Airborne Instrumentation for Astronomy IX. SPIE, Bellingham, p. 121846H
Hayes C. R. et al., 2023, ApJ, 955, 17
Heger A., Woosley S. E., 2010, ApJ, 724, 341
Heger A., Woosley S., Vo P., Chen K., Joggerst C., 2012, in Aoki W., Ishigaki M., Suda T., Tsujimoto T., Arimoto N.eds, ASP Conf. Series Vol. 458, Galactic Archaeology: Near-Field Cosmology and the Formation of the Milky Way., San Francisco. p. 11
Helmi A., Babusiaux C., Koppelman H. H., Massari D., Veljanoski J., Brown A. G. A., 2018, Nature, 563, 85
Hopkins P. F. et al., 2018, MNRAS, 480, 800
Horta D. et al., 2021, MNRAS, 500, 1385
Horta D. et al., 2023, MNRAS, 520, 5671
Howes L. M. et al., 2014, MNRAS, 445, 4241
Howes L. M. et al., 2015, Nature, 527, 484
Howes L. M. et al., 2016, MNRAS, 460, 884
Ireland M. J., White M., Bento J. P., Farrell T., Labrie K., Luvaul L., Nielsen J. G., Simpson C., 2018, in Guzman J. C., Ibsen J.eds, SPIE Conf. Series Vol. 10707, Software and Cyberinfrastructure for Astronomy V. SPIE, Bellingham. p 1070735
Ishigaki M. N., Aoki W., Arimoto N., Okamoto S., 2014, A&A, 562, A146
Ishigaki M. N., Tominaga N., Kobayashi C., Nomoto K., 2018, ApJ, 857, 46
Ivanova D. V., Shimanskiĭ V. V., 2000, Astron. Rep., 44, 376
Izutani N., Umeda H., Tominaga N., 2009, ApJ, 692, 1517
Jeong M., Lee Y. S., Beers T. C., Placco V. M., Kim Y. K., Koo J.-R., Lee H.-G., Yang S.-C., 2023, ApJ, 948, 38
Ji A. P., Frebel A., Ezzeddine R., Casey A. R., 2016, ApJ, 832, L3
Ji A. P., Simon J. D., Frebel A., Venn K. A., Hansen T. T., 2019, ApJ, 870, 83
Ji A. P. et al., 2020, ApJ, 889, 27
Johnston K. V., Bullock J. S., Sharma S., Font A., Robertson B. E., Leitner S. N., 2008, ApJ, 689, 936
Jönsson H. et al., 2020, AJ, 160, 120
Karlsson T., Bromm V., Bland-Hawthorn J., 2013, Rev. Mod. Phys., 85, 809
Kielty C. L. et al., 2021, MNRAS, 506, 1438
Koch A., McWilliam A., Grebel E. K., Zucker D. B., Belokurov V., 2008, ApJ, 688, L13
Koch A., Feltzing S., Adén D., Matteucci F., 2013, A&A, 554, A5
Koch A., McWilliam A., Preston G. W., Thompson I. B., 2016, A&A, 587, A124
Kramida A., Ralchenko Yu., Reader J., NIST ASD Team, 2021, NIST Atomic Spectra Database (ver. 5.9), National Institute of Standards and Technology, Gaithersburg, MD
Labrie K., Anderson K., Cárdenes R., Simpson C., Turner J. E. H., 2019, in Teuben P. J., Pound M. W., Thomas B. A., Warner E. M.eds, ASP Conf. Series Vol. 523, Astronomical Data Analysis Software and Systems XXVII. Astron. Soc. Pac., San Francisco. p. 321
Lamb M. et al., 2017, MNRAS, 465, 3536
Lawler J. E., Bonvallet G., Sneden C., 2001a, ApJ, 556, 452
Lawler J. E., Wickliffe M. E., den Hartog E. A., Sneden C., 2001b, ApJ, 563, 1075
Lawler J. E., Guzman A., Wood M. P., Sneden C., Cowan J. J., 2013, ApJS, 205, 11
Lawler J. E., Wood M. P., Den Hartog E. A., Feigenson T., Sneden C., Cowan J. J., 2014, ApJS, 215, 20
Lawler J. E., Sneden C., Cowan J. J., 2015, ApJS, 220, 13
Lawler J. E., Sneden C., Nave G., Den Hartog E. A., Emrahoğlu N., Cowan J. J., 2017, ApJS, 228, 10
Lawler J. E., Hala Sneden C., Nave G., Wood M. P., Cowan J. J., 2019, ApJS, 241, 21
Limongi M., Chieffi A., 2018, ApJS, 237, 13
Lind K., Bergemann M., Asplund M., 2012, MNRAS, 427, 50
Lucchesi R. et al., 2022, MNRAS, 511, 1004
Lucey M. et al., 2019, MNRAS, 488, 2283
Lucey M. et al., 2021, MNRAS, 501, 5981
Lucey M. et al., 2022, MNRAS, 509, 122
McConnachie A. W. et al., 2022, in Evans C. J., Bryant J. J., Motohara K.eds, SPIE Conf. Ser. Vol. 12184, Ground-based and Airborne Instrumentation for Astronomy IX. SPIE, Bellingham. p. 121841E
Mardini M. K., Frebel A., Chiti A., Meiron Y., Brauer K. V., Ou X., 2022, ApJ, 936, 78
Marigo P., Girardi L., Bressan A., Groenewegen M. A. T., Silva L., Granato G. L., 2008, A&A, 482, 883
Martin N. F. et al., 2022, Nature, 601, 45
Mashonkina L. I., Belyaev A. K., 2019, Astron. Lett., 45, 341
Mashonkina L., Jablonka P., Pakhomov Y., Sitnova T., North P., 2017a, A&A, 604, A129

Downloaded from https://academic.oup.com/mnras/article/528/3/4838/7602409 by guest on 21 April 2024

Mashonkina L., Jablonka P., Sitnova T., Pakhomov Y., North P., 2017b, A&A, 608, A89
Mashonkina L. et al., 2023, MNRAS, 523, 2111
Masseron T. et al., 2014, A&A, 571, A47
Meléndez J., Barbuy B., 2009, A&A, 497, 611
Mucciarelli A., Bellazzini M., Massari D., 2021, A&A, 653, A90
Ness M. et al., 2013a, MNRAS, 430, 836
Ness M. et al., 2013b, MNRAS, 432, 2092
Ness M., Debattista V. P., Bensby T., Feltzing S., Roškar R., Cole D. R., Johnson J. A., Freeman K., 2014, ApJ, 787, L19
Norris J. E., Wyse R. F. G., Gilmore G., Yong D., Frebel A., Wilkinson M. I., Belokurov V., Zucker D. B., 2010, ApJ, 723, 1632
Pazder J., Fournier P., Pawluczyk R., van Kooten M., 2014, in Navarro R., Cunningham C. R., Barto A. A.eds, SPIE Conf. Ser. Vol. 9151, Advances in Optical and Mechanical Technologies for Telescopes and Instrumentation. SPIE, Bellingham. p. 915124
Pazder J. et al., 2020, in SPIE Conf. Ser., SPIE, Bellingham. p. 1144743
Pignatari M., Gallino R., Meynet G., Hirschi R., Herwig F., Wiescher M., 2008, ApJ, 687, L95
Placco V. M., Frebel A., Beers T. C., Stancliffe R. J., 2014, ApJ, 797, 21
Placco V. M., Sneden C., Roederer I. U., Lawler J. E., Den Hartog E. A., Hejazi N., Maas Z., Bernath P., 2021, Res. Notes Am. Astron. Soc., 5, 92
Plez B., 2012, Astrophysics Source Code Library, record ascl:1205.004
Reggiani H., Schlaufman K. C., Casey A. R., Ji A. P., 2020, AJ, 160, 173
Reichert M., Hansen C. J., Hanke M., Skúladóttir Á., Arcones A., Grebel E. K., 2020, A&A, 641, A127
Roederer I. U., 2017, ApJ, 835, 23
Roederer I. U., Lawler J. E., 2012, ApJ, 750, 76
Roederer I. U., Lawler J. E., 2021, ApJ, 912, 119
Ruffoni M. P., Den Hartog E. A., Lawler J. E., Brewer N. R., Lind K., Nave G., Pickering J. C., 2014, MNRAS, 441, 3127
Salvadori S., Bonifacio P., Caffau E., Korotin S., Andreevsky S., Spite M., Skúladóttir Á., 2019, MNRAS, 487, 4261
Santistevan I. B., Wetzel A., Sanderson R. E., El-Badry K., Samuel J., Faucher-Giguère C.-A., 2021, MNRAS, 505, 921
Schiavon R. P. et al., 2017, MNRAS, 466, 1010
Schlaufman K. C., Casey A. R., 2014, ApJ, 797, 13
Schultheis M., Rich R. M., Origlia L., Ryde N., Nandakumar G., Thorsbro B., Neumayer N., 2019, A&A, 627, A152
Schultz G. V., Wiemer W., 1975, A&A, 43, 133
Sestito F. et al., 2019, MNRAS, 484, 2166
Sestito F. et al., 2020, MNRAS, 497, L7
Sestito F. et al., 2021, MNRAS, 500, 3750
Sestito F. et al., 2023a, MNRAS, 518, 4557
Sestito F. et al., 2023b, MNRAS, 525, 2875
Sitnova T. M. et al., 2021, MNRAS, 504, 1183
Sneden C. A., 1973, PhD thesis, The University of Texas at Austin
Sobeck J. S., Lawler J. E., Sneden C., 2007, ApJ, 667, 1267
Sobeck J. S. et al., 2011, AJ, 141, 175
Spite M. et al., 2006, A&A, 455, 291
Starkenburg E., Oman K. A., Navarro J. F., Crain R. A., Fattahi A., Frenk C. S., Sawala T., Schaye J., 2017a, MNRAS, 465, 2212
Starkenburg E. et al., 2017b, MNRAS, 471, 2587
Stetson P. B., Pancino E., 2008, Publ. Astron. Soc. Pac., 120, 1332
Suda T. et al., 2008, PASJ, 60, 1159
Takahashi K., Yoshida T., Umeda H., 2018, ApJ, 857, 111
Taylor M. B., 2005, in Shopbell P., Britton M., Ebert R.eds, ASP Conf. Series Vol. 347, Astronomical Data Analysis Software and Systems XIV. Astron. Soc. Pac., San Francisco. p. 29
Tissera P. B., White S. D. M., Scannapieco C., 2012, MNRAS, 420, 255
Tumlinson J., 2010, ApJ, 708, 1398
Venn K. A., Irwin M., Shetrone M. D., Tout C. A., Hill V., Tolstoy E., 2004, AJ, 128, 1177
Venn K. A. et al., 2012, ApJ, 751, 102
Venn K. A. et al., 2020, MNRAS, 492, 3241
Vitali S. et al., 2022, MNRAS, 517, 6121
Waller F. et al., 2023, MNRAS, 519, 1349
Wenger M. et al., 2000, A&AS, 143, 9
White S. D. M., Springel V., 2000, in Weiss A., Abel T. G., Hill V.eds, The First Stars. Springer-Verlag, Berlin. p. 327
Wise J. H., Turk M. J., Norman M. L., Abel T., 2012, ApJ, 745, 50
Wolf C. et al., 2018, Publ. Astron. Soc. Aust., 35, e010
Wood M. P., Lawler J. E., Sneden C., Cowan J. J., 2013, ApJS, 208, 27
Wood M. P., Lawler J. E., Sneden C., Cowan J. J., 2014, ApJS, 211, 20
Wood M. P., Sneden C., Lawler J. E., Den Hartog E. A., Cowan J. J., Nave G., 2018, ApJS, 234, 25
Youakim K. et al., 2017, MNRAS, 472, 2963

SUPPORTING INFORMATION

Supplementary data are available at *MNRAS* online.

suppl_data

Please note: Oxford University Press is not responsible for the content or functionality of any supporting materials supplied by the authors. Any queries (other than missing material) should be directed to the corresponding author for the article.

[1]*Department of Physics and Astronomy, University of Victoria, PO Box 3055, STN CSC, Victoria BC V8W 3P6, Canada*
[2]*NRC Herzberg Astronomy & Astrophysics, 5071 West Saanich Road, Victoria, BC V9E 2E7, Canada*
[3]*Institute of Astronomy, University of Cambridge, Madingley Road, Cambridge CB3 0HA, UK*
[4]*Laboratoire d'astrophysique, École Polytechnique Fédérale de Lausanne (EPFL), Observatoire, CH-1290 Versoix, Switzerland*
[5]*GEPI, Observatoire de Paris, Université PSL, CNRS, 5 Place Jules Janssen, F-92195 Meudon, France*
[6]*Université de Strasbourg, CNRS, Observatoire astronomique de Strasbourg, UMR 7550, F-67000 Strasbourg, France*
[7]*Max-Planck-Institut für Astronomie, Königstuhl 17, D-69117 Heidelberg, Germany*
[8]*Kapteyn Astronomical Institute, University of Groningen, Landleven 12, NL-9747AD Groningen, the Netherlands*
[9]*Instituto de Estudios Astrofísicos, Universidad Diego Portales, Av. Ejército Libertador 441, Santiago, Chile*
[10]*Gemini Observatory/NSF's NOIRLab, Casilla 603 La Serena, Chile*
[11]*Dipartimento di Fisica G. Occhialini, Universitá degli Studi di Milano Bicocca, Piazza della Scienza 3, I-20126 Milano, Italy*
[12]*Australian Astronomical Observatory*
[13]*Australian Astronomical Optics, Macquarie University, 105 Delhi Rd, North Ryde, NSW 2113, Australia*
[14]*Research School of Astronomy and Astrophysics, College of Science, Australian National University, Canberra 2611, Australia*

This paper has been typeset from a TEX/LATEX file prepared by the author.

© 2024 The Author(s).
Published by Oxford University Press on behalf of Royal Astronomical Society. This is an Open Access article distributed under the terms of the Creative Commons Attribution License (http://creativecommons.org/licenses/by/4.0/), which permits unrestricted reuse, distribution, and reproduction in any medium, provided the original work is properly cited.

Downloaded from https://academic.oup.com/mnras/article/528/3/4838/7602409 by guest on 21 April 2024